

Efficient and Interpretable Infrared and Visible Image Fusion Via Algorithm Unrolling

Zixiang Zhao, Shuang Xu, Chunxia Zhang, Junmin Liu, and Jiangshe Zhang*

School of Mathematics and Statistics, Xi'an Jiaotong University, China
 zixiangzhao@stu.xjtu.edu.cn, shuangxu@stu.xjtu.edu.cn,
 cxzhang@mail.xjtu.edu.cn, junminliu@mail.xjtu.edu.cn,
 jszhang@mail.xjtu.edu.cn.

Abstract. Infrared and visible image fusion expects to obtain images that highlight thermal radiation information from infrared images and texture details from visible images. In this paper, an interpretable deep network fusion model is proposed. Initially, two optimization models are established to accomplish two-scale decomposition, separating low-frequency base information and high-frequency detail information from source images. The algorithm unrolling that each iteration process is mapped to a convolutional neural network layer to transfer the optimization steps into the trainable neural networks, is implemented to solve the optimization models. In the test phase, the two decomposition feature maps of base and detail are merged respectively by the fusion layer, and then the decoder outputs the fusion image. Qualitative and quantitative comparisons demonstrate the superiority of our model, which is interpretable and can robustly generate fusion images containing highlight targets and legible details, exceeding the state-of-the-art methods.

Keywords: Image Fusion, Two-Scale Decomposition, Algorithm Unrolling.

1 Introduction

Image fusion, as an image enhancement technology, is a hot issue in image processing research community. By merging the images obtained by different sensors on the same scene, we expect to obtain images that highlight the advantages of each source image and are robust to perturbations at the same time. Image fusion can effectively improve the utilization of image information, eliminate conflicts and redundancies between multiple sensors, while forming a clear and complete description of targets to facilitate recognition and tracking in subsequence [28]. Infrared and visible image fusion, abbreviated as IVIF, is a typical topic in image fusion. By incorporating prior knowledge to the images during the preprocessing stage, IVIF is effective to make full use of information in images and widely used in fire control [16], autonomous driving [21] and face recognition[24], etc.

Commonly, the infrared image is used to characterize the heat of objects, which is strongly robust to illumination changes and artifacts. Targets in the

infrared image are usually highlighted and easy to distinguish from the environment. However, the texture and gradient information are seriously lost, and the spatial resolution is low. Hence, it is difficult to make satisfactory descriptions of the target details. In contrast, the visible image is good at keeping the information of gradient and pixel intensity and displaying the brightness of objects. The content and objects can be described with enriched details and high resolution. However, as it is easily affected by illumination changes and light reflection, objects are difficult to be extracted from the background. IVIF aims at generating fusion images with both detailed texture information and highlight radiation information so as to form a clear, complete and accurate description of the targets, which is significant for the tracking and identification image tasks [24].

Recent IVIF algorithms can be divided into classic methods and deep learning (DL)-based methods. Multi-scale decomposition (MSD) is one of the most promising techniques among classic methods. It usually separates an image into multiple-level images based on some criteria and uses a specific merging strategy to fuse the separated images at different levels. Finally the fusion image can be obtained by adding the decomposed images of each level together [20]. Among the decomposition methods, filters [35] and transformers (e.g., wavelet[22] and curvelet[6]) are the most frequently employed. The difficulty of MSD is how to design reasonable decomposition algorithms and fusion strategies.

With the development of DL in the field of computer vision, deep neural networks (DNNs) have been widely used in the IVIF task due to their strong feature extraction capability. DL-based methods can be divided into three categories: pre-trained model class, generative adversarial net (GAN) class, and auto-encoder (AE) class. The first class is the combination of MSD and DL [19,17]. After MSD, the base images are weighted averaged. Then, the detail images with high-frequency information are fused by a pre-trained neural network (such as VGG-19 [33]). The second class is the GAN-based method. In FusionGAN [27], the image fusion task is described as an adversarial game. The generator generates an image with the advantages of two source images. The discriminator adds detail information to the fusion image by forcing the generator to output the image similar to the source visible image. Recently, DPAL [25] improves the quality of detailed information in fusion images by means of detail loss and target edge-enhancement loss. The third class is to train an AE network, in which the encoder and decoder are responsible for feature extraction and image reconstruction. For example, Densefuse [18] trains an AE network with dense blocks [13]. In the test phase, the feature maps of the source images extracted by encoder are fused by weighted-average, and the fused image is obtained by the decoder. In general, DL-based methods are more effective than classic methods for strong feature extraction ability.

The existing DL-based models for the IVIF task are data-driven but lack of interpretability. In this paper, by the principle of algorithm unrolling, we extend an optimization-based two-scale decomposition algorithm into an interpretable DNN, named by Algorithm Unrolling Image Fusion (AUIF). Our contributions are as follows:

(1) Firstly, we propose a new two-scale decomposition framework by formulating two optimization models separately extracting base and detail images. By the principle of algorithm unrolling, the update steps are mapped to a novel AE network. In this fashion, the proposed optimization models and their hyperparameters can be trained end-to-end by the back-propagation algorithm.

(2) The current methods [24,18,39,19] use only a part of images in the TNO dataset for testing, where the scene is limited to the nightlight illumination. To make a convincing evaluation, we employ 132 test pictures from TNO, NIR, and FLIR datasets with diverse scenes. The complicated lighting conditions and various objects make the test scenario more comprehensive. Compared with eight state-of-the-art (SOTA) algorithms, the qualitative and quantitative results on the test datasets imply that our method has the best performances and it can stably generate fusion images with sharpen edges and abundant details in all the three datasets.

The rest of this paper consists of the following sections. We briefly review the related work in section 2. Then in section 3, the formulation and implementation of our model are introduced. The results of intensive experiments are reported in section 4. Finally, we give conclusions in section 5.

2 Related Work

Currently, many IVIF algorithms have been proposed, and MSD is one of the most promising techniques. Its basic idea is to decompose the original picture into a group of images, each of which contains unique characters. Instead of directly fusing the original pictures, MSD first decompose the original images into different scales, and then the fused images are obtained by performing the inverse MSD. The popular decomposition methods include pyramid transform [5], discrete cosine transform [15], nonsubsampled contourlet transform [38] and bilateral filter [12].

Two classes of DL-based methods are closely related with MSD. The first one incorporates pre-trained DNNs in an image fusion pipeline. But it is found that this technique is not an end-to-end procedure and less effective. The other one is the AE networks based method. Actually, the decomposed images can be regarded as feature maps, while MSD and inverse MSD correspond to encoder and decoder, respectively. Therefore, in the era of DL, MSD is progressively replaced by AE networks. The representative models are dense block based AE [18] and U-net’s variant [14]. Compared with manually designed MSD methods, the data-driven AE networks are more flexible but lack of interpretability.

Recently, an emerging technique called algorithm unrolling provides an encouraging pipeline to design interpretable DNNs. One of the seminal work is the fast sparse coding proposed by Gregor and LeCun [9]. The traditional sparse coding problem is solved by iterative algorithms. And the idea of algorithm unrolling is to extend the iterative algorithm’s computational graph into a DNN, in which the pre-defined hyperparameters and unknown coefficients can be trained

end-to-end. The algorithm unrolling based DL is very competitive with high interpretability and less number of parameters [29].

3 Method

This section formulates a new image composition model and then this algorithm is unrolled to a neural network.

3.1 Motivation

For the current IVIF algorithms, it is difficult for the classic methods to separate the low-frequency base information and high-frequency detail information by means of simple filters, manually-designed optimization models or transformers. As for most of the DL-based methods, they are black-box and lack of interpretability. Currently, their working mechanism still remains unclear.

Accordingly, we propose an optimization-based image decomposition model to decompose a photo into a base image and a detail image. And we aim to unroll this optimization algorithm as a trainable deep network with high interpretability.

3.2 Optimization Model

For an image I , its base image corresponds to the low-frequency background information, and can be obtained by solving the following problem:

$$B^* = \arg \min L_B = \arg \min \left\{ \frac{\theta_B}{2} \|I - B\|_F^2 + \sum_{j=1}^n \|g_j^B * B\|_F^2 \right\}, \quad (1)$$

where B^* is the base image, $g_j^B (j = 1, \dots, n)$ are high-pass filters, $*$ represents the convolution operation, and θ_B is a hyperparameter. In Eq. (1), the first part is the data fidelity term and the second part is a regularizer to extract the high-frequency from B . The detail layer D^* is with high-frequency detail information, and it can be also acquired by a similar optimization problem:

$$D^* = \arg \min L_D = \arg \min \left\{ \frac{\theta_D}{2} \|I - D\|_F^2 + \sum_{j=1}^n \|g_j^D * D\|_F^2 \right\}, \quad (2)$$

where $g_j^D (j = 1, \dots, n)$ are low-pass filters, and θ_D is a hyperparameter.

We use the gradient descent algorithm to solve above problems. For model (1), the gradient of L_B can be calculated as:

$$\frac{\partial L_B}{\partial B} = -\theta_B (I - B) + \sum_{j=1}^n (g_j^B)^\top * (g_j^B * B). \quad (3)$$

So the update rule of gradient descent is:

$$B^{out} = B^{in} - \eta_B \left[\sum_{j=1}^n (g_j^B)^\top * (g_j^B * B^{in}) - \theta_B (I - B^{in}) \right], \quad (4)$$

where η_B is the step size. For model (2), its update rule can be derived in a similar way.

3.3 Algorithm Unrolling

BCL and DCL. Inspired by the work [34], we transform the optimization problem as a convolutional neural network (CNN). Replace the filters $\{g_j^B, g_j^D\}$ by convolutional units and the update process (Eq. (4)) can be rewritten as

$$B^{out} = B^{in} - \eta_B [Conv_2^B (Conv_1^B (B^{in})) - \theta_B (I - B^{in})], \quad (5)$$

where $Conv_i^B (i = 1, 2)$ denotes the convolutional unit with a kernel of size k . In this paper, k is set to 3. Similarly, the update of the detail feature map can be expressed as:

$$D^{out} = D^{in} - \eta_D [Conv_2^D (Conv_1^D (D^{in})) - \theta_D (I - D^{in})]. \quad (6)$$

In what follows, Eqs. (5) and (6) are named by Base Convolutional Layer (BCL) and Detail Convolution Layer (DCL), respectively. To keep the spatial size unchanged and prevent artifacts at the image edges, the input of BCL and DCL is reflection-padded. To further enhance feature extraction capability, the output passes through a batch normalization layer and is activated by a parametric rectified linear unit (PReLU). It is worth pointing out that the filters $\{g^B, g^D\}$, step sizes $\{\eta_B, \eta_D\}$, and hyperparameters $\{\theta_B, \theta_D\}$ in Eqs. (4) and (5) are pre-defined in traditional algorithms, while they are learnable in our proposed BCL and DCL.

Network Architecture. Actually, both base and detail images can be regarded as feature maps of the source image I . We thus stack N BCLs and DCLs as two encoders to extract base and detail feature maps. In addition, the two feature maps are added and pass through a decoder to recover the source image I , and the reconstructed image can be denoted by \hat{I} .

The network architecture in training phase is displayed in Figure 1(a), a single DCL is shown in Figure 1(b) and a BCL has the same structure with different parameters. The number of channels (c^{input}, c^{output}) for the first convolution units (i.e., $Conv_1^B$ and $Conv_1^D$) is $(1, C)$. As for the second convolutional units (i.e., $Conv_2^B$ and $Conv_2^D$), it is set as $(C, 1)$. In this paper, C is set to 64. There are no shared parameters in BCL and DCL. The input of base and detail encoders B_0 and D_0 are initialized by applying blur and Laplacian filters, respectively. As for the decoder, it consists of a convolution unit, batch regularization layer, and the sigmoid function. The number of both input and output channels of the convolution unit are 1. The role of sigmoid is to make the pixel values in the reconstructed image range from 0 to 1.

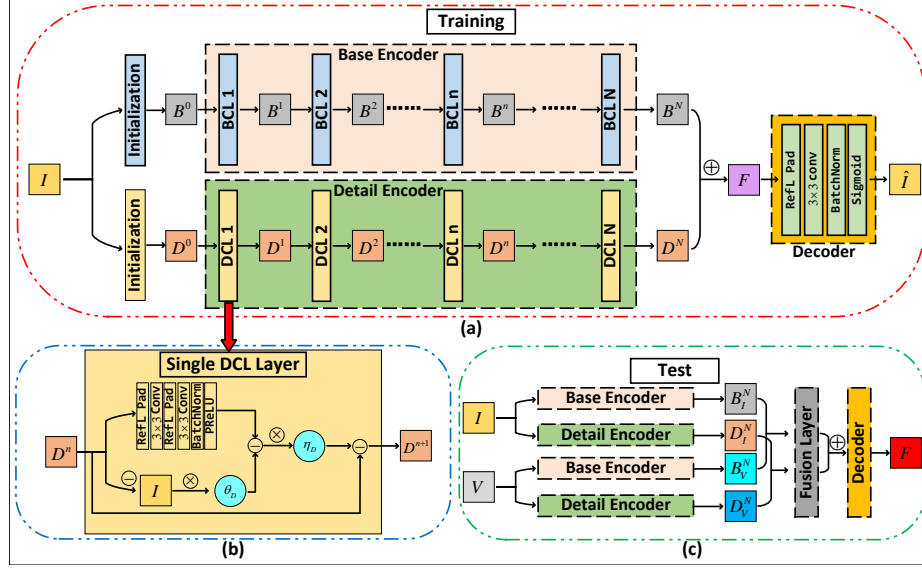


Fig. 1. Illustration of the AUIF model. (a): Network framework of AUIF in training phase; (b): Display of a single DCL in the AUIF model, the same structure is also contained in BCL with different parameters; (c): Network framework of AUIF in test phase.

Loss Function. For the reconstruction loss of the AUIF network, it is defined by

$$L_{total} = L_2(I, \hat{I}) + \mu L_{SSIM}(I, \hat{I}) = \left\| I - \hat{I} \right\|_2^2 + \mu \frac{1 - SSIM(I, \hat{I})}{2}, \quad (7)$$

where μ is the tuning parameter, SSIM is the structural similarity index [37] which measures the similarity between two images. In Eq. (7), the L_2 loss ensures that the pixel intensity of the reconstructed image is close to the source image, while the SSIM loss makes the reconstructed image approximate the source image in terms of brightness, structure and contrast.

Test. After training, we can get two encoders (decomposers) and a decoder (reconstructor). In the test phase, we fuse the paired infrared and visible images. Fig. 1(c) shows the specific workflow. Here, $\{B_I^N, D_I^N\}$ denote the base and detail feature maps of infrared images generated by N th BCL and DCL, while $\{B_V^N, D_V^N\}$ represent those of visible images.

In the test phase, we need to set a fusion layer between the encoder and decoder to merge B_I^N, B_V^N and D_I^N, D_V^N respectively. $\Gamma(\cdot)$ is used to represent pixel-wise operations in the fusion layer, and it is defined by

$$\begin{aligned} B^N(x, y) &= \Gamma(B_I^N, B_V^N) = \alpha_I^B(x, y) \times B_I^N(x, y) + \alpha_V^B(x, y) \times B_V^N(x, y), \\ D^N(x, y) &= \Gamma(D_I^N, D_V^N) = \alpha_I^D(x, y) \times D_I^N(x, y) + \alpha_V^D(x, y) \times D_V^N(x, y). \end{aligned} \quad (8)$$

Table 1. Information of Datasets in this paper.

| Dataset | Training | | Validation | | Test | | |
|---------------|------------|-----------|------------|-------|-----------|-------------|--|
| | FLIR-Train | Urban-NIR | Street-NIR | TNO | FLIR-Test | Country-NIR | |
| Illumination | Day&Night | Day | Day | Night | Day&Night | Day | |
| # Image pairs | 180 | 58 | 50 | 40 | 40 | 52 | |

Three commonly used fusion strategies $\Gamma_i(\cdot)$ ($i = 1, 2, 3$) are listed as follows:

- Addition: $\alpha_I^B = \alpha_V^B = \alpha_I^D = \alpha_V^D = 1$.
- Average: $\alpha_I^B = \alpha_V^B = \alpha_I^D = \alpha_V^D = 0.5$.
- L_1 -attention Addition: Inspired by the work of [18], L_1 norm can reflect the salience degree of pixels. Thus we perform L_1 norm operation on the base and detail feature maps, based on which the adding weight can be calculated. The weights of base feature maps is defined by

$$\alpha_I^B(x, y) = \frac{\chi(\|B_I^N(x, y)\|_1)}{\chi(\|B_I^N(x, y)\|_1) + \chi(\|B_V^N(x, y)\|_1)}, \alpha_V^B(x, y) = 1 - \alpha_I^B(x, y) \quad (9)$$

where $\chi(\cdot)$ is the 3×3 blur filter. The weights of detail feature maps α_I^D and α_V^D can be calculated similarly.

4 Experiments

In this section, a series of experiments are conducted to study the behavior of our AUIF network. Experiments are implemented with Pytorch on a computer with Intel Core i7-9750H CPU@2.60GHz and RTX2070 GPU.

4.1 Datasets and Metrics

Datasets. Our experiments use three IVIF datasets: TNO¹ [36], FLIR² and NIR³ [4]. The basic information is reported in Table 1. Note that the FLIR dataset is randomly divided into the training set and the test set.

Metrics. In order to quantitatively describe the effect of fusion, we selected six metrics: entropy (EN)[32], standard deviation (SD)[31], spatial frequency (SF)[8], visual information fidelity (VIF)[11], average gradient (AG)[7] and sum of the correlations of differences (SCD)[1]. EN and SD measure the amount of information contained in fusion images. SF and AG reflect the detail and texture

¹ <https://figshare.com/articles/TNOImageFusionDataset/1008029>

² <https://github.com/jiayi-ma/RoadScene>

³ https://ivrlwww.epfl.ch/supplementary_material/cvpr11/index.html

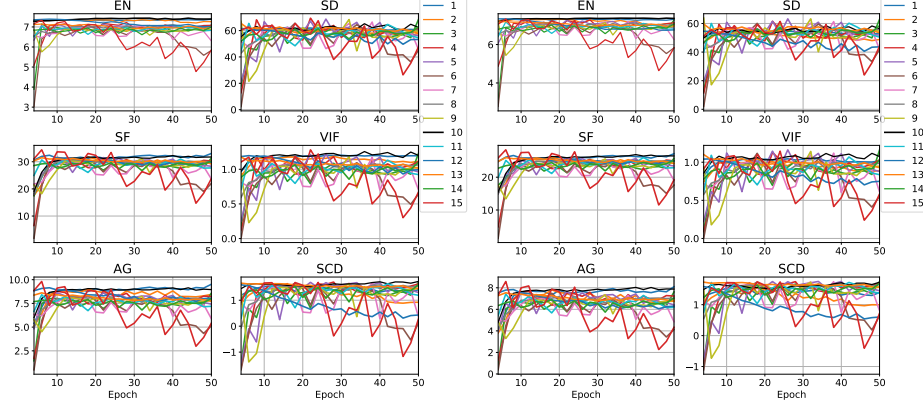


Fig. 2. The results of verifying the number of BCL/DCL layers in validation datasets Urban-NIR (left) and Street-NIR (right).

information of fusion images. VIF reports the consistency degree with the human visual system and SCD implies the agreement between source and fusion images. The higher the value, the better the quality of the fused results. More calculation details of the metrics can be found in [26].

4.2 Implementation Details and Network Configuration

In this experiment, we set the tuning parameter μ of Eq. (7) to 5. The AUIF network is trained over 80 epochs with a batch size of 32. The learning rate is 10^{-2} for the first 40 epochs and it is decreased to 10^{-3} for the rest epochs. The training samples are randomly cropped to 128×128 .

For the learnable parameters η and θ in Eq. (5) and (6), η_b and η_d are randomly initialized with a normal distribution $\mathcal{N}(0.1, 0.03^2)$, while θ_b and θ_d are set to 10^{-3} and 1, respectively. The configuration of θ is related to B^0 and D^0 . The initial detail feature map D^0 is generated by the Laplacian filter, and it is found that D^0 visually differs from the original image I . Thus, a larger θ_d is needed for sake of data fidelity. In contrast, the initial base feature map B^0 is generated by the blur filter, and it is very similar to the source image. So, a smaller θ_b is needed to prevent from learning redundant features. At last, the number of layers N is determined on validation set. We vary N from 1 to 15, and the results are reported in Fig. 2. It is found that $N = 10$ strikes the balance among six metrics on both Urban-NIR and Street-NIR datasets. The loss, η and θ curves versus the epoch index are displayed in Fig. 3. It is shown that our network can converge rapidly with above configuration.

4.3 Experimental Results

Experiments on Fusion Layer. Firstly, we need to choose a proper fusion layer on the validation set. The results of the three strategies in the Street

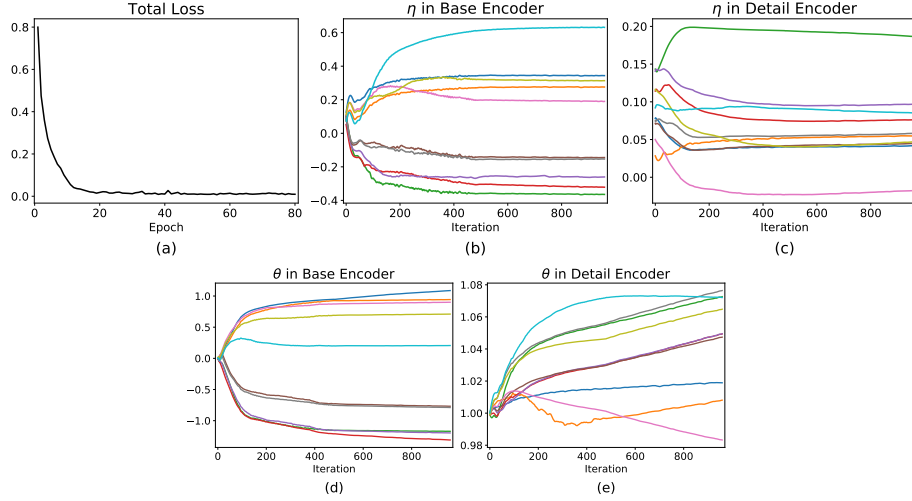


Fig. 3. Exhibition of training results. (a): The loss curve in 80 epochs. (b) & (d): η_B & θ_B changes of each BCL layer in the Base Encoder. (c) & (e): η_D & θ_D changes of each DCL layer in the Detail Encoder.

Table 2. Results on validation datasets. The best values are highlighted in bold.

| NIR Dataset. Scene: Street | | | | | | |
|----------------------------|------------------|-------------------|-------------------|------------------|------------------|------------------|
| Strategy | EN | SD | SF | VIF | AG | SCD |
| Add | 7.04±0.19 | 53.68±2.00 | 24.71±1.24 | 0.97±0.07 | 7.03±0.53 | 1.55±0.12 |
| Ave | 6.86±0.03 | 36.01±0.98 | 17.05±0.24 | 0.63±0.02 | 4.92±0.08 | 0.70±0.08 |
| L_1 -Att | 6.88±0.05 | 36.90±2.29 | 17.43±1.39 | 0.57±0.08 | 5.00±0.44 | 0.56±0.30 |
| NIR Dataset. Scene: Urban | | | | | | |
| Strategy | EN | SD | SF | VIF | AG | SCD |
| Add | 7.03±0.21 | 59.17±2.50 | 29.97±1.32 | 1.07±0.09 | 8.09±0.57 | 1.47±0.15 |
| Ave | 7.10±0.04 | 40.96±0.84 | 20.58±0.29 | 0.76±0.02 | 5.91±0.11 | 0.20±0.13 |
| L_1 -Att | 7.09±0.08 | 41.31±1.63 | 20.68±0.87 | 0.74±0.05 | 5.92±0.28 | 0.11±0.25 |

and Urban scenery of the NIR dataset are shown in Table 2. Obviously, the addition strategy reaches higher values on all metrics. Therefore, in the following experiments, we utilize the addition strategy.

Image Decomposition Effect. We test whether the AUIF network can generate satisfactory base and detail feature maps. Three representative cases are displayed in Fig. 4. It is shown that the initial base feature maps B^0 are very blurred, and the final base feature maps B^N contain more textures, clear structure and high contrast. For the detail feature maps, the initial ones D^0 only

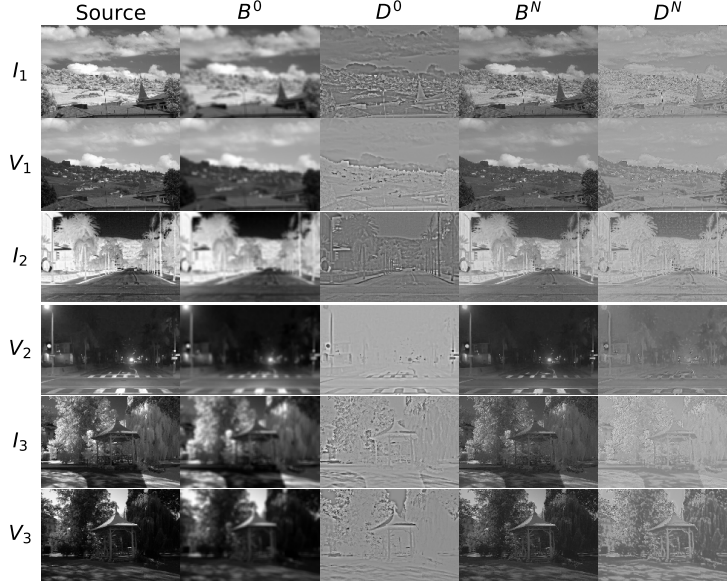


Fig. 4. Display of the decomposition effect. From left to right: source image, initial input of BCL and DCL, base feature map and detail feature map output by the encoder, respectively.

include a part of unclear edges. Conversely, in the final maps D^N , the overall profiles are sharpened, and the interested targets are highlighted. In summary, the decomposed feature maps meet our demands, since the low-frequency and high-frequency information are fully expressed on the two kinds of feature maps.

Qualitative Comparison. We compare our AUIF with eight SOTA methods, including ADF [2], CSR [23], DeepFuse [30], Densefuse [18], FusionGAN [27], ImageFuse [19], TSIFVS [3] and TVADMM [10]. Representative fusion results are shown in Fig. 5.

We simply divide test samples into three categories: individuals, stuffs, and scenery. For individuals, our fusion images can reveal the specular lighting of targets, more details and clearer infrared radiation information. For stuffs, our method can make interested ones be with sharpening edges. As a result, it is easy to distinguish the stuffs from the background. For scenery, our results are clearer and have high contrast. Furthermore, the details of small objects are easier to observe. In conclusion, our model can retain both thermal radiation information and visible detail texture information.

Quantitative Comparison. Besides qualitative comparison, we use six metrics to quantitatively evaluate the performance of all methods. The results of the

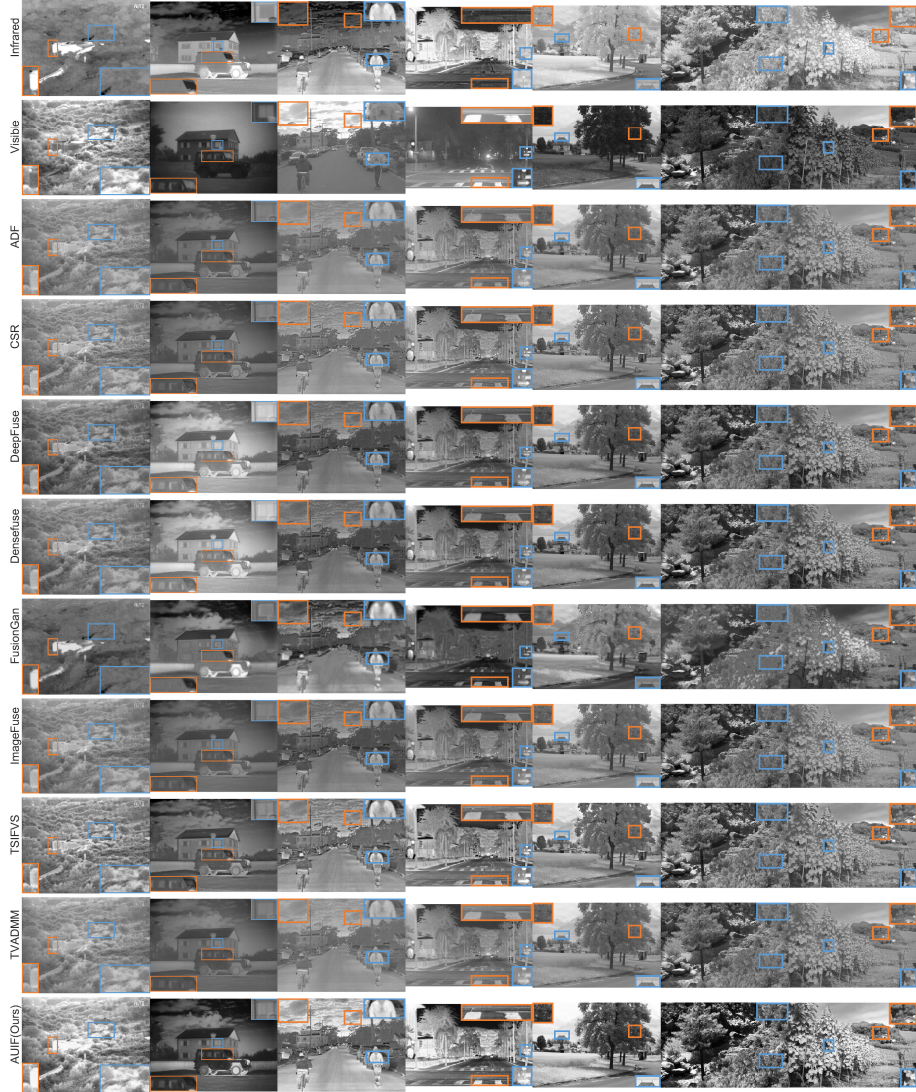


Fig. 5. Exhibition of qualitative comparison results. From top to bottom: infrared images, visible images, results of SOTA methods and our method.

three test datasets are exhibited in Table 3. It is shown that our method achieves excellent results on all test datasets with regard to all metrics. However, others may perform well on a certain dataset with regard to part of metrics. It proves that our method is suitable for the IVIF task under various illuminations and scenes.

Table 3. Quantitative results of the SOTA methods in test datasets. The best and the second best values are highlighted by bold typeface and underline, respectively.

| Methods | Dataset: TNO image fusion dataset | | | | | |
|-----------|------------------------------------|----------------|----------------|---------------|---------------|---------------|
| | EN | SD | SF | VIF | AG | SCD |
| ADF | 6.3994 | 22.9633 | 10.7819 | 0.2862 | 2.9877 | 1.6051 |
| CSR | 6.4279 | 23.6032 | 11.4450 | 0.3117 | 3.3670 | 1.6252 |
| DeepFuse | <u>6.8598</u> | <u>32.2485</u> | 11.1250 | <u>0.5812</u> | 3.5987 | <u>1.8049</u> |
| DenseFuse | 6.8425 | 31.8171 | 11.0946 | 0.5716 | 3.5966 | 1.7983 |
| FusionGan | 6.5761 | 29.0352 | 8.7621 | 0.2575 | 2.4169 | 1.3955 |
| ImageFuse | 6.3821 | 22.9376 | 9.8005 | 0.3060 | 2.7187 | 1.6190 |
| TSIFVS | 6.6685 | 28.0364 | <u>12.5984</u> | 0.4560 | <u>3.9799</u> | 1.6790 |
| TV-admm | 6.4022 | 23.0066 | 9.0339 | 0.2836 | 2.5175 | 1.6042 |
| Ours | 7.0217 | 42.1322 | 13.6589 | 0.6921 | 4.4443 | 1.8583 |
| Methods | Dataset: FLIR image fusion dataset | | | | | |
| | EN | SD | SF | VIF | AG | SCD |
| ADF | 6.7982 | 28.3711 | 14.4801 | 0.3373 | 3.5640 | 1.3902 |
| CSR | 6.9085 | 30.5294 | 17.1279 | 0.3733 | 4.7995 | 1.4184 |
| DeepFuse | <u>7.2134</u> | <u>37.3506</u> | 15.4709 | 0.4984 | 4.8021 | 1.7153 |
| DenseFuse | 7.2127 | 37.3154 | 15.4956 | 0.4982 | 4.8222 | <u>1.7158</u> |
| FusionGan | 7.0167 | 34.3834 | 11.5071 | 0.2893 | 3.2046 | 1.1815 |
| ImageFuse | 6.9918 | 32.5792 | 14.5194 | 0.4194 | 4.1496 | 1.5709 |
| TSIFVS | 7.1520 | 35.8887 | <u>18.7940</u> | <u>0.5034</u> | <u>5.5679</u> | 1.4968 |
| TV-admm | 6.7972 | 28.0715 | 14.0436 | 0.3251 | 3.5240 | 1.4042 |
| Ours | 7.4644 | 48.9926 | 20.2932 | 0.6322 | 5.9091 | 1.8649 |
| Methods | Dataset: NIR image fusion dataset | | | | | |
| | EN | SD | SF | VIF | AG | SCD |
| ADF | 7.1053 | 38.9776 | 17.3125 | 0.5384 | 5.3809 | 1.0911 |
| CSR | 7.1697 | 40.3827 | 20.3697 | 0.5831 | 6.4876 | 1.1230 |
| DeepFuse | 7.3033 | 45.8152 | 18.6271 | 0.6765 | 6.1781 | 1.3656 |
| DenseFuse | <u>7.3045</u> | <u>45.8496</u> | 18.7179 | 0.6774 | 6.2277 | <u>1.3675</u> |
| FusionGan | 7.0555 | 34.9118 | 14.3088 | 0.4243 | 4.5642 | 0.5057 |
| ImageFuse | 7.2168 | 42.3072 | 18.3599 | 0.6129 | 5.9203 | 1.2224 |
| TSIFVS | 7.2999 | 43.7430 | <u>20.6455</u> | <u>0.6879</u> | <u>6.8225</u> | 1.1944 |
| TV-admm | 7.1291 | 40.4688 | 16.6853 | 0.5297 | 5.3186 | 1.0904 |
| Ours | 7.3883 | 61.8759 | 28.5219 | 1.0373 | 9.3274 | 1.6946 |

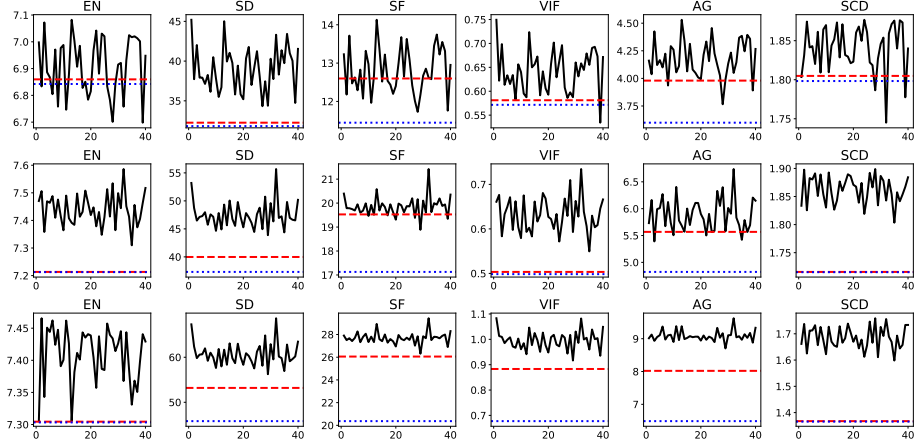


Fig. 6. The results of 40 parallel training. From top to bottom, the rows correspond to the results on TNO, FLIR and NIR, respectively.

Experiments on Robustness. To test the stability and reproducibility of our model, we repeatedly trained the AUIF network 40 times, and metric curves of the 40 models are shown in Fig. 6. To facilitate comparison, the top two values provided by eight competitors are set as baselines (see the red and blue dashed lines). It is observed that the AUIF network is a robust and good performer.

5 Conclusion

We design a novel deep fusion network by combining the interpretability of optimization models and the strong feature extraction capability of deep neural networks. Firstly, two optimization models are established to make the two-scale decomposition. Inspired by the idea of algorithm unrolling, the iteration steps of the optimization models can be extended to a neural network. Numerous experiments conducted on TNO, FLIR and NIR datasets demonstrate that our model can robustly generate satisfactory fusion images.

References

1. Aslantas, V., Bendes, E.: A new image quality metric for image fusion: the sum of the correlations of differences. *AEU - International Journal of Electronics and Communications* **69**(12), 1890–1896 (2015)
2. Bavirisetti, D.P., Dhuli, R.: Fusion of infrared and visible sensor images based on anisotropic diffusion and karhunen-loeve transform. *IEEE Sensors Journal* **16**(1), 203–209 (2015)
3. Bavirisetti, D.P., Dhuli, R.: Two-scale image fusion of visible and infrared images using saliency detection. *Infrared Phys. & Techn.* **76**, 52–64 (2016)

4. Brown, M.A., Süsstrunk, S.: Multi-spectral SIFT for scene category recognition. In: The 24th IEEE Conference on Computer Vision and Pattern Recognition, CVPR 2011, Colorado Springs, CO, USA, 20-25 June 2011. pp. 177–184. IEEE Computer Society (2011)
5. Bulanon, D., Burks, T., Alchanatis, V.: Image fusion of visible and thermal images for fruit detection. *Biosystems Engineering* **103**(1), 12 – 22 (2009)
6. Choi, M., Kim, R.Y., Nam, M.R., Kim, H.O.: Fusion of multispectral and panchromatic satellite images using the curvelet transform. *IEEE Geoscience and Remote Sensing Letters* **2**(2), 136–140 (2005)
7. Cui, G., Feng, H., Xu, Z., Li, Q., Chen, Y.: Detail preserved fusion of visible and infrared images using regional saliency extraction and multi-scale image decomposition. *Optics Communications* **341**, 199–209 (2015)
8. Eskicioglu, A.M., Fisher, P.S.: Image quality measures and their performance. *IEEE Transactions on Communications* **43**(12), 2959–2965 (1995)
9. Gregor, K., LeCun, Y.: Learning fast approximations of sparse coding. In: Fürnkranz, J., Joachims, T. (eds.) *Proceedings of the 27th International Conference on Machine Learning (ICML-10)*, June 21-24, 2010, Haifa, Israel. pp. 399–406. Omnipress (2010)
10. Guo, H., Ma, Y., Mei, X., Ma, J.: Infrared and visible image fusion based on total variation and augmented lagrangian. *Journal of the Optical Society of America A* **34**(11), 1961–1968 (2017)
11. Han, Y., Cai, Y., Cao, Y., Xu, X.: A new image fusion performance metric based on visual information fidelity. *Information fusion* **14**(2), 127–135 (2013)
12. Hu, J., Li, S.: The multiscale directional bilateral filter and its application to multisensor image fusion. *Information Fusion* **13**(3), 196 – 206 (2012)
13. Huang, G., Liu, Z., Van Der Maaten, L., Weinberger, K.Q.: Densely connected convolutional networks. In: CVPR. pp. 4700–4708 (2017)
14. Jian, L., Yang, X., Liu, Z., Jeon, G., Gao, M., Chisholm, D.: A symmetric encoder-decoder with residual block for infrared and visible image fusion. *CoRR* **abs/1905.11447** (2019)
15. Jin, X., Jiang, Q., Yao, S., Zhou, D., Nie, R., Lee, S.J., He, K.: Infrared and visual image fusion method based on discrete cosine transform and local spatial frequency in discrete stationary wavelet transform domain. *Infrared Physics & Technology* **88**, 1 – 12 (2018)
16. Lahoud, F., Süsstrunk, S.: Ar in vr: Simulating infrared augmented vision. In: ICIP. pp. 3893–3897. IEEE (2018)
17. Lahoud, F., Süsstrunk, S.: Fast and efficient zero-learning image fusion. *arXiv preprint arXiv:1905.03590* (2019)
18. Li, H., Wu, X.J.: Densefuse: A fusion approach to infrared and visible images. *IEEE TIP* **28**(5), 2614–2623 (2018)
19. Li, H., Wu, X., Kittler, J.: Infrared and visible image fusion using a deep learning framework. In: 24th International Conference on Pattern Recognition, ICPR 2018, Beijing, China, August 20-24, 2018. pp. 2705–2710. IEEE Computer Society (2018)
20. Li, S., Yang, B., Hu, J.: Performance comparison of different multi-resolution transforms for image fusion. *Information Fusion* **12**(2), 74–84 (2011)
21. Li, Y., Zhao, H., Hu, Z., Wang, Q., Chen, Y.: Irvfusenet: Fusion of infrared and visible light images for depth prediction. *Information Fusion* **58**, 1–12 (2020)
22. Liu, Y., Jin, J., Wang, Q., Shen, Y., Dong, X.: Region level based multi-focus image fusion using quaternion wavelet and normalized cut. *Signal Processing* **97**, 9–30 (2014)

23. Liu, Y., Chen, X., Ward, R.K., Wang, Z.J.: Image fusion with convolutional sparse representation. *IEEE Signal Processing Letters* **23**(12), 1882–1886 (2016)
24. Ma, J., Chen, C., Li, C., Huang, J.: Infrared and visible image fusion via gradient transfer and total variation minimization. *Information Fusion* **31**, 100–109 (2016)
25. Ma, J., Liang, P., Yu, W., Chen, C., Guo, X., Wu, J., Jiang, J.: Infrared and visible image fusion via detail preserving adversarial learning. *Information Fusion* **54**, 85–98 (2020)
26. Ma, J., Ma, Y., Li, C.: Infrared and visible image fusion methods and applications: A survey. *Information Fusion* **45**, 153–178 (2019)
27. Ma, J., Yu, W., Liang, P., Li, C., Jiang, J.: Fusiongan: A generative adversarial network for infrared and visible image fusion. *Information Fusion* **48**, 11–26 (2019)
28. Meher, B., Agrawal, S., Panda, R., Abraham, A.: A survey on region based image fusion methods. *Information Fusion* **48**, 119–132 (2019)
29. Monga, V., Li, Y., Eldar, Y.C.: Algorithm unrolling: Interpretable, efficient deep learning for signal and image processing. *CoRR* **abs/1912.10557** (2019)
30. Prabhakar, K.R., Srikan, V.S., Babu, R.V.: Deepfuse: A deep unsupervised approach for exposure fusion with extreme exposure image pairs. In: *ICCV*. pp. 4724–4732 (2017)
31. Rao, Y.J.: In-fibre bragg grating sensors. *Measurement Science and Technology* **8**(4), 355 (1997)
32. Roberts, J.W., Van Aardt, J.A., Ahmed, F.B.: Assessment of image fusion procedures using entropy, image quality, and multispectral classification. *Journal of Applied Remote Sensing* **2**(1), 023522 (2008)
33. Simonyan, K., Zisserman, A.: Very deep convolutional networks for large-scale image recognition. *arXiv preprint arXiv:1409.1556* (2014)
34. Sreter, H., Giryes, R.: Learned convolutional sparse coding. In: *2018 IEEE International Conference on Acoustics, Speech and Signal Processing, ICASSP 2018, Calgary, AB, Canada, April 15-20, 2018*. pp. 2191–2195. IEEE Computer Society (2018)
35. Toet, A.: Image fusion by a ratio of low-pass pyramid. *Pattern Recognition Letters* **9**(4), 245–253 (1989)
36. Toet, A., Hogervorst, M.A.: Progress in color night vision. *Optical Engineering* **51**(1), 1 – 20 (2012)
37. Wang, Z., Bovik, A.C., Sheikh, H.R., Simoncelli, E.P., et al.: Image quality assessment: from error visibility to structural similarity. *IEEE TIP* **13**(4), 600–612 (2004)
38. Xiang, T., Yan, L., Gao, R.: A fusion algorithm for infrared and visible images based on adaptive dual-channel unit-linking pcnn in nsct domain. *Infrared Physics & Technology* **69**, 53 – 61 (2015)
39. Zhang, X., Ma, Y., Fan, F., Zhang, Y., Huang, J.: Infrared and visible image fusion via saliency analysis and local edge-preserving multi-scale decomposition. *Journal of the Optical Society of America A* **34**(8), 1400–1410 (2017)